Nanoarchitectonic Engineering of Thermal-Responsive Magnetic Nanorobot Collectives for Intracranial Aneurysm Therapy

WILEY-VCH

Nanoarchitectonic Engineering of Thermal-Responsive Magnetic Nanorobot Collectives for Intracranial Aneurysm Therapy

Jienan Wang, Qi Zhou, Qi Dong, Jian Shen, Junnian Hao, Dong Li, Tiantian Xu, Xiaojun Cai, Wenkun Bai, Tao Ying, Yuehua Li, Li Zhang, Yueqi Zhu, Longchen Wang,* Jianrong Wu,* and Yuanyi Zheng**

J. Wang, Q. Dong, J. Shen, J. Hao, X. Cai, W. Bai, T. Ying, L. Wang, J. Wu, Y. Zheng

Department of Ultrasound in Medicine, Shanghai Institute of Ultrasound in Medicine, Shanghai Sixth People's Hospital Affiliated to Shanghai Jiao Tong University School of Medicine, Shanghai, 200233, P. R. China

E-mail: wanglch09@sjtu.edu.cn; wujianrong028@shsmu.edu.cn; zhengyuanyi@sjtu.edu.cn

L. Zhang

Department of Mechanical and Automation Engineering

The Chinese University of Hong Kong, Hong Kong, P. R. China

D. Li, T. Xu

Guangdong Provincial Key Laboratory of Robotics and Intelligent System

Shenzhen Institute of Advanced Technology, Chinese Academy of Sciences, Shenzhen, 518055, P. R. China

J. Wang, Y. Li, Y. Zhu

Department of Radiology, Shanghai Sixth People's Hospital Affiliated to Shanghai Jiao Tong University School of Medicine, Shanghai, 200233, P. R. China

E-mail: zhuyueqi@sjtu.edu.cn

Q. Dong

Department of Ultrasound, Ren Ji Hospital, Shanghai Jiao Tong University School of Medicine, Shanghai, 200002, P. R. China

Q. Zhou

School of Engineering, The University of Edinburgh, Edinburgh, EH9 3FB, UK

Keywords: Intracranial aneurysm, embolization therapy, magnetic nanorobots, targeted drug delivery, endovascular treatment

Abstract

Stent-assisted coiling is a main treatment modality for intracranial aneurysms (IAs) in clinics, but critical challenges remain to be overcome, such as exogenous implant-induced stenosis and reliance on antiplatelet agents. Herein, we report an endovascular approach for IA therapy without stent grafting or microcatheter shaping, enabled by active delivery of thrombin (Th) to target aneurysms using innovative phase-change material (PCM)-coated magnetite-thrombin (Fe_3O_4-Th@PCM) FTP nanorobots. The nanorobots are controlled by an integrated actuation system of dynamic torque-force hybrid magnetic fields. With robust intravascular navigation guided by real-time ultrasound imaging, nanorobotic collectives can effectively accumulate and retain in model aneurysms constructed *in vivo*, followed by controlled release of the encapsulated Th for rapid occlusion of the aneurysm upon melting the protective PCM (thermally responsive in a tunable manner) through focused magnetic hyperthermia. Complete and stable aneurysm embolization was confirmed by postoperative examination and 2-week postembolization follow-up using digital subtraction angiography (DSA), contrast-enhanced ultrasound (CEUS) and histological analysis. The safety of the embolization therapy was assessed through biocompatibility evaluation and histopathology assays. Our strategy, seamlessly integrating secure drug packaging, agile magnetic actuation and clinical interventional imaging, avoids possible exogenous implant rejection, circumvents cumbersome microcatheter shaping, and offers a promising option for IA therapy.

1. Introduction

Ruptured intracranial aneurysms (IAs) are the leading cause of subarachnoid hemorrhage, which is a condition associated with high mortality[1] and a main type of stroke, one of the top three causes of death and disability combined worldwide[2]. Timely intervention of aneurysms has been proven key to reducing mortality and complications[3], primarily in the form of surgical interventions or endovascular treatments[4-6]. Whereas the former are often limited by significant trauma and slower recovery, the latter provide alternative approaches prone to lower-degree of invasiveness and faster recovery. The International Subarachnoid Aneurysm Trial (ISAT) Collaborative Group reported that the absolute risk of endovascular therapy decreased by 7.4% compared with surgical clipping and achieved better outcomes in independent survival[7]. Although endovascular treatments (e.g., through coiling embolization) demonstrate a higher possibility of rebleeding than neurosurgical clipping, they usually pose lower risks[6] and are better tolerated in patients over 80 years old[8]. Therefore, the current clinical paradigm for IA treatment has gradually shifted from open surgery to endovascular embolization in a majority of cases[5, 9].

Existing endovascular treatment options mainly include coil embolization, stent-assisted coiling and flow diverter stent implantation[10]. Both coil embolization and stent-assisted coiling are revolutionary innovations, but with their own limitations at the moment. For example, it is difficult for the coils to compactly fill the entire aneurysm cavity in a complete manner, and the mass effect of giant aneurysms may compress the peripheral nerve structure, leading to neurological dysfunction. Flow diverter stents remain an influential treatment option for IA therapy[4, 11], and are primarily used for some giant and uncoilable wide-necked aneurysms on the internal carotid artery. However, the long time for introducing thrombosis in the aneurysm risks undesirable rebleeding. Another drawback of using flow diverters is the potential embolization of the perforated artery, which can lead to ischemic complications [9]. For the treatment of IAs, stents as exogenous implants also inevitably induce platelet aggregation, causing thrombosis and intimal hyperplasia, and eventually leading to vascular stenosis or occlusion. Furthermore, to avoid stent restenosis, long-term intake of oral antiplatelet agents is required, which remains a main challenge[12]. In addition, flow diverters cannot be applied to ruptured aneurysms when antiplatelet is contraindicated[13].

There is still a significant unmet need for new strategies to effectively and safely embolize aneurysms while reducing the use of exogenous implanted materials for IA therapy[14, 15]. Previous studies have innovated the use of hydrogel or similar embolic agents[16-18] to embolize aneurysms, but further preclinical developments and clinical trials are needed. On the other

hand, thrombin (Th), a principal clotting factor in the human body capable of eliciting immediate thrombosis through activating the platelets in blood and converting the circulating fibrinogen to fibrin, has been clinically exploited in other pathologies, e.g., for the treatment of pseudoaneurysms treatments[19, 20]. Ultrasound-guided Th injection for pseudoaneurysms achieved a primary success rate of 97% accompanied by low-rate complications[21, 22]. However, a targeted Th delivery system for achieving precise, rapid and stable aneurysm embolization in the main arteries has yet to be developed.

Micro/nanorobots are capable of performing complex tasks in bodily fluids and have been extensively explored as a candidate for disease diagnosis, drug delivery, thrombolytic therapy, minimally invasive surgery, and so on[23-25]. Until now, diverse types of micro/nanorobots have been designed or constructed to achieve efficient locomotion in biofluidic environments, either driven by internal chemical reactions or external physical stimuli (e.g., light, ultrasound, electric, and magnetic fields)[26-29]. Among others, magnetic actuation exhibits desirable controllability as well as biocompatibility, and has been one of the most commonly employed approach in biomedical applications, especially for targeted drug delivery[30-39]. Ideally, miniature magnetic robots can be manipulated to accumulate near a target location for biomedical operations, such as the controlled release of cargos (e.g., drugs, imaging agents, and proteins), provided that the ambient environment does not impose substantial disturbances to the magnetically controlled microrobots. Recently, selective embolization of targeted regions of a vasculature *in vivo* (about 50 mm in diameter) has also been achieved using microrobotic swarms without the need for active navigation, through a magnetic actuation strategy to maintain the swarm integrity of magnetic particles at vascular junctions[40]. Compared to traditional drug delivery strategies, magnetic actuation-mediated targeted delivery is a promising approach for improving delivery efficiency and reducing side effects on normal tissues/organs[41-44].

Inspired by the above progress in applying magnetic micro/nanorobots for biomedicine, we set out to exploit an integrated approach of localized drug delivery and minimally-invasive endovascular treatment for potential IA therapy. In contrast to the recently investigated application of micro/nanorobots in thrombolysis (i.e., dissolving thrombi), we herein propose active deployment of thermal-responsive magnetic nanorobot collectives to induce rapid embolization of target aneurysms in situ without the need for stent-implantation or microcatheter shaping **(Figure 1)**. As a proof of concept, the constituent nanoparticle Fe_3O_4-Th@PCM (FTP) of the nanorobot collectives is designed on the basis of three functional units, including a magnetite (Fe_3O_4) core to enable magnetic actuation, a payload of encapsulated Th to induce thrombosis upon release in the aneurysm and a phase-change material (PCM)

protective coating to avoid unintended drug leakage in blood. Given that conventional endovascular therapy allows for rapid and high-volume delivery of drugs, our injection of FTP nanorobots takes advantage of a balloon microcatheter operated in the upstream parent artery of the aneurysm to facilitate targeted delivery with reduced drug depletion into the blood circulation. Under the focusing effect of our customized magnetic actuation system that generates a dynamic torque-force hybrid field, the FTP nanorobots can assemble into robust collectives and navigate toward the targeted aneurysm for accumulation and retention. Upon stimulation by an alternating magnetic field (AMF) device, localized magnetic hyperthermia is induced to melt the PCM coating and release the loaded Th on the collectives for rapid embolization of the aneurysm. Digital subtraction angiography (DSA) and contrast-enhanced ultrasound imaging (CEUS) are then performed to evaluate the patency of the aneurysm sac and validate the embolization state under dynamic conditions. The safety of this strategy is also demonstrated through systematic biocompatibility evaluation and histopathology assays. Our proposed strategy integrates a magnetic actuation-enabled therapeutic system with localized drug release and improved delivery efficiency for promising IA therapy without using stent-implantation, therefore easing the challenges confronted by current endovascular treatments. We have verified this strategy *in vivo* using model aneurysms constructed on the common carotid artery (CCA) of rabbits and conducted all procedures in clinical interventional environment, which helps bridge the potential gap to realize bench to bed translation.

2. Results

2.1. Fabrication of PCM-coated magnetite-thrombin (Fe_3O_4-Th@PCM) FTP nanorobots

The central design of the FTP nanorobots is utilizing thermally responsive phase-change materials for co-encapsulating Fe_3O_4 nanoparticles and thrombin molecules in compact form (**Figure 1a**), to integrate magnetic swarming locomotion and targeted drug delivery aimed at intracranial aneurysm therapy (**Figure 1e**). The Fe_3O_4 nanoparticles were synthesized using a typical solvothermal method[45], with characteristic spherical shapes of approximately 205 nm in diameter (**Figure S1**). The PCM was fabricated by mixing oleic acid and 1-hexadecanol as reported in our previous work[46], and has a tunable melting point ranging from 41.4 to 49.3 °C as the mass ratio varies between 1:2 and 1:5 (oleic acid/1-hexadecanol) **(Figure S2a)**. Then the FTP was synthesized using the Fe_3O_4 nanoparticles, PCM and Th via a resolidification method detailed in the Experimental Section. In the present work, we have adopted a mass ratio of 1:2.5 for the PCM with a corresponding melting point of 42.5 °C **(Figure S2b)** given that overly high temperature (e.g., exceeding 45 °C) could thermally denaturized the encapsulated Th. Indeed,

transmission electron microscopy (TEM) imaging verifies that the PCM coating of the synthesized FTP would melt and the FTP disintegrates subject to 5 min incubation at 43 °C **(Figure S2c)**, thus suggesting that magnetic hyperthermia could trigger the release of the encapsulated Th. More details about the materials, fabrication methods and structural characterization of the FTP can be found in the Supplementary Methods and Figures of the Supporting Information (SI), including Fourier Transform Infrared Spectroscopy (FTIR, **Figure S3a**), X-ray Diffraction (XRD, **Figure S3b**) and X-ray Photoelectron Spectroscopy (XPS, **Figure S4a-d**).

TEM imaging shows that the fabricated FTP particles as nanorobots possess a spherical shape with a mean diameter of 295 nm and demonstrate a clear presence of PCM coating **(Figure 1b)**. When dispersed in water, the FTP nanoparticles have a mean hydrodynamic diameter of 311.2 ± 5.9 nm **(Figure 1c)** and can remain stable in phosphate buffered saline (PBS) with negligible changes in size after 7 days of incubation **(Figure S5a)**. Furthermore, the FTP nanoparticles are stable at room temperature and cause no hemolysis even at a high concentration of 5 mg ml^{-1} **(Figure S5b)**. The percentage of Th content in the fabricated FTP nanoparticles can be estimated as 15.3% (w/w%) (calculation details in the Supplementary Methods of the SI), where the concentration of Th was determined through a standard curve of absorption intensity with a Bradford protein assay evaluating the Th adsorption (**Figure S6**)[47]. From the magnetization curve measured by a vibrating sample magnetometer (VSM), the FTP nanoparticles demonstrate typical superparamagnetic behavior with a saturation magnetization value of 47.9 emu g^{-1} **(Figure 1d)**, which is high to facilitate efficient actuation and locomotion using magnetic fields.

The magnetic hyperthermia properties of the FTP nanoparticles were evaluated *in vitro* first using an AMF device that generate alternating magnetic field for inducive heating. To reflect typical *in vivo* aneurysm environments, the FTP dispersion volume for the *in vitro* experiments was set as 140 µl based on estimate for a hypothesized aneurysm with a diameter of 6.5 mm. FTP dispersions of varying concentrations were mixed with either PBS or fresh rabbit arterial blood and then placed under the AMF coil for 5 min treatment **(Figure 2a)**. The thermal images **(Figure 2b)** and the corresponding temperature-change profiles **(Figures 2c and d)** reveal good magnetothermal effects of the FTP, with evident rise in temperature of the mixture against treatment time. Notably, the temperature rise behaves in an FTP concentration-dependent manner, with considerable elevation of approximately 28.6 °C in the PBS mixture **(Figure 2c)** and 27.2 °C in the blood mixture **(Figure 2d)** at an FTP concentration of 20 mg ml^{-1} (after 5min AMF treatment), which should suffice to trigger collapse of the PCM coating

(melting point 42.5 °C) on the FTP particles to release the encapsulated Th. Indeed, the release curve of Th measured for the FTP-PBS mixture (20 mg ml^{-1}) demonstrates a surge in the Th concentration after 3 min AFM treatment (**Figure 2e**); prior to 3 min, negligible Th release can be detected, indicating a gradual heating process by AMF to melt the PCM for Th release. Therefore, the FTP concentration 20 mg ml^{-1} is adopted for subsequent experiments on *in vitro* and *in vivo* aneurysm models. As comparison, the magnetic hyperthermia properties of Fe_3O_4, Fe_3O_4@PCM (FP) were also investigated (**Figure S7a**), which are in line with the FTP behavior demonstrated above (**Figures S7b-e).**

To evaluate the coagulation performance, mixtures of different formulations (Fe_3O_4, FP, Th and FTP) with fresh rabbit arterial blood (1 ml) with or without AMF treatment were placed in 3.5 cm petri dish for coagulation assay (**Figures 2a and f**). The amount of Th (15 μg) in the control group was determined using the Th release curve in **Figure 2e**. As shown in **Figure 2f**, only the Th group or FTP plus AMF treatment group have thrombi formed, whereas no coagulation could be observed in the other groups. In addition, the strength of the formed thrombi appear dose-dependent (**Figures S8a and 9**). We further compare the stability of the thrombi formed by Th and FTP, which both maintain integrity within a testing window of 60 h (**Figure S8b**), therefore confirming that the FTP can induce the formation of stable thrombi that last for extended periods of time. The stiffness and elasticity of the formed blood clots were also investigated, which revealed similar structural properties between the FTP and Th groups (**Figure S10**).

2.2. *In Vitro* Locomotion and Hyperthermia of FTP Nanorobot Collectives

Given the workspace required for practical aneurysm treatment of animals or humans, we employ a customized magnetic actuation system integrating quadruple magnet modules on a rotatory motor (**Figures S11a and 12a**). This integrated actuation system we recently developed [44] can provide dynamic torque-force hybrid magnetic fields for on-demand locomotion of the FTP nanorobots under low-field strength through the rotation and displacement of the motor. While the rotation of the motor at designated frequencies induces a rotating magnetic field to assemble (e.g., at 3-4 Hz) or disperse the nanorobots (e.g., at 12 Hz), the displacement of the motor guides the locomotion of the nanorobots via the pulling force arising from the magnetic field gradient [44]. The magnetic field strength decreases in general as the distance between the actuation system and the target site increases (**Figure S12b**), and at an operating distance of 3 cm the magnetic field gradient for generating pulling force can be as large as 1250 mT/m according to simulation of the three-dimensional (3D) magnetic field

(**Figure S13**). To demonstrate the locomotion capability of the formed FTP nanorobot collectives under the hybrid magnetic field, we perform *in vitro* experiments using 3D-printed channels of "W", "S" and "R" shaped designs to mimic complex environments in curved or branched blood vessels (**Figure 3a, Figures S14 and 15, Supplementary Video 1**). Evidently, the FTP nanorobots can be robustly assembled into a stable collective and navigate the channel under the rotating magnetic field (3 Hz, 15 mT). We further imitate high-flowrate conditions in the parent artery of potential aneurysms (real-time flow velocity up to 12 cm s^{-1}, typical values measured under anesthesia conditions from the internal carotid artery of human with a 6 mm aneurysm[48]) by using a "Y" shaped bifurcation consisting of three channels. The assembling effect of the magnetic actuation systems is found weakened at excessively high flow rates, but the actuated FTP nanorobots could be satisfactorily guided to enter the target channel at flow rates up to 6 cm s^{-1} (**Figure S16**).

We next verify whether a magnetic pulling force could promote FTP nanorobot accumulation toward a target aneurysm under arterial flow conditions in the order of centimeters per second. A classic aneurysm model[16] is constructed by connecting a saccular cavity onto a straight channel (**Figure 3b-i and Figure S17a**). The aspect ratio (AR) of a saccular aneurysm, defined as the ratio of its perpendicular height to its neck diameter (**Figure 3b-i**), is a widely used clinical metric to mark the aneurysm state and predict the risk of its rupture[49]. To determine parameters for subsequent experimental investigation, preliminary flow simulations using COMSOL finite-element models are conducted to analyze the flow field and particle trajectories around a fairly deep aneurysm (AR = 1.5) for a range of flow rates (velocities up to 12 cm s^{-1}), with or without magnetic pulling (**Figure 3c, Figure S18 and Supplementary Video 2**). The simulations reveal that it is difficult or impossible for the particles to naturally flow into the aneurysm without magnetic actuation (**Figure S18b**). In contrast, most particles enter the aneurysm with an active magnetic force applied, achieving satisfactory particle accumulation at flow velocities up to 5 cm s^{-1} (**Figure S18c**).

Since the simulations support the feasibility of accumulating FTP nanorobots toward the aneurysm through magnetic actuation, *in vitro* experiments (**Figure S19**) were conducted in transparent resin aneurysm replicas with AR ranging from 1.9 (for a deep sac) to 0.7 (for a shallow sac) under a moderate flow velocity of 2.5 cm s^{-1} (**Figure 3d and Supplementary Video 3**). The accumulation of FTP nanorobot collectives in the aneurysm is found to decrease as the sac becomes shallower, indicated by the captured Fe content measured after each experiment using inductively coupled plasma–optical emission spectrometry (ICP–OES) (**Figure 3h**). Thermal images of the aneurysm subject to FTP accumulation reveal that

substantial elevation of the local temperature can be achieved through AMF-induced magnetic hyperthermia, achieving a net temperature change up to 25 °C within 5 min (**Figures 3e and i**). The magnetothermal effect is weakened under higher flow rates but can still effectively elevate the temperature for about 10-15 °C in a flow of 5 cm s^{-1} and 5-10 °C in flows of 7-12 cm s^{-1} in a fairly deep sac (AR = 1.9) (**Figure S20**). For the shallowest aneurysm (AR = 0.7), local temperature elevation is still possible but would be unsatisfactory under excessively high flow conditions (e.g., 2-3 °C only in flows of 7-12 cm s^{-1}) (**Figure S21**). More complex aneurysm replicas reflecting other clinically observed aneurysms have also been assessed, such as a lobular aneurysm with daughter sacs and a branching aneurysm on the vascular bifurcation (**Figures 3b-ii, b-iii, f and g, Figures S17b-c, Figure S22 and Supplementary Video 4**). In the majority of cases, adequate particle accumulation in the aneurysm is attainable at low to moderate flow rates for effective magnetic hyperthermia and temperature elevation.

We further investigate the effective range of our current magnetic actuation system (operating at a low magnetic field strength, 15 mT) for accumulating FTP nanorobots in the target aneurysm at varying distances, given that realistic IAs may be located in different depths of the brain, either close to or distant from the skull (**Figure S23a**). The temperature elevation in the aneurysm decreases against the operating distance but can be compensated by prolonged AMF treatment (**Figures S23b and c**). Even at a large operating distance of 5 cm, FTP accumulates for efficient hyperthermia to achieve 20 °C temperature rise in about 1 min under reduced flow conditions (flow rate: 0.5 cm s^{-1}) (**Figure S23b**). Overall, the FTP nanorobots can be assembled into collectives and perform controlled locomotion toward the aneurysm under magnetic manipulation for hyperthermia treatment and associated Th release, provided that the blood flow is not excessively high (e.g., below 6 cm s^{-1}) and the operating distance is fairly close to the aneurysm (e.g., 2-5 cm). Given the low-strength magnetic field (15 mT) currently applied, physiological flow rates in arteries (*ca.* 10-20 cm/s) are attainable with an enhanced actuation system of the same design but hosting stronger magnets.

2.3. *In Vivo* Evaluation of Embolization Treatment in a Rabbit Carotid Aneurysm Model

After characterizing the collective motion and magnetic hyperthermia properties of the FTP nanorobots *in vitro*, followed by cytotoxicity assessments (to be detailed in the next section), we proceed to evaluate their efficacy of inducing occlusion and embolization treatment with an *in vivo* aneurysm model (**Figure 4a**). We first constructed sidewall aneurysms via surgery on the rabbit carotid artery (**Figure S24a**). Then with the aid of DSA fluoroscopy, an intermediate catheter was placed at the proximal end of the artery and a balloon catheter was employed to

temporarily block the proximal blood flow. Then, 1.5 ml 20 mg ml^{-1} dispersion of FTP in PBS (totaling 30 mg FTP, the determination of this *in vivo* safe dose is detailed in the Supplementary Methods of the SI) was injected through the balloon catheter into the artery, and the FTP nanorobots were magnetically guided toward the aneurysm by the actuation system applying a rotating magnetic field (3Hz, 15mT). Effective locomotion of the nanorobot collectives was achieved *in vivo*, capable of traveling over a distance of about 2.5 cm (**Figure S24b and Supplementary Video 5**). They also showed robust reconfiguration capability by crossing a narrowed region of the artery subject to stenosis (artificially introduced by partial ligation) under real-time ultrasound imaging feedback (**Figure 4b and Supplementary Video 6**).

Once all available FTP nanorobots are accumulated in the aneurysm sac without freely flowing particles in the blood stream of the parent artery based on the ultrasound imaging feedback, AMF was performed to release the encapsulated Th for embolization in situ. The peak temperature was maintained below 50 °C, which is a critical heating threshold that may lead to potential thermal damage to the aneurysm and surrounding tissues[50]. As monitored by the infrared camera, a rapid rise in temperature (taking 14 s only from 32 to 44 °C) beyond the melting point of PCM can be attained at the central region of the aneurysm *in vivo* (**Figure 4c and Figure S25**). Note the much quicker melting of PCM under AFM treatment here in comparison to the petri dish tests (**Figure 2**) is due to the higher ambient temperature and weaker heat dissipation in the rabbit internal environment. Through comparing the DSA and 3D-DSA images of the aneurysm before and after the embolization treatment, evident occlusion of the aneurysm is found to have been introduced, as indicated by absence of the treated aneurysm sac in angiogram (**Figures 4d-e and Supplementary Video 7**). Agreeing results were observed in repeated experiments with other rabbits (**Figure S 26**). CEUS was also applied to assess changes in the aneurysm sac (**Figure 4f, Figure S27 and Supplementary Video 8**). In both the transverse and sagittal planes, the aneurysm shows plentiful blood flow before treatment but absence of flow signal immediately after the treatment, therefore confirming the embolization efficacy of the FTP nanorobots. Furthermore, follow-up DSA evaluation after two weeks of treatment demonstrate that no recanalization of the aneurysm occurs (**Figure S28**).

As the control group, FTP nanorobots were injected into the artery without magnetic actuation (**Figure 5a**), and the Fe content in the aneurysm sac was measured by ICP–OES after experiment for both groups. In contrast to the high Fe level (33.2 ± 4.7 ID% g^{-1}) detected in the aneurysm treated with magnetically guided FTP nanorobots, the Fe level in the control group is much lower (< 10 ID% g^{-1}, **Figure 5b**). The *in vivo* delivery efficiency of FTP nanorobots under magnetic actuation was assessed to be 32.3% based on the captured Fe content and the

total mass injected (n = 3), thus accounting for one third of the injected sample containing *ca.* 4.3×10^{11} nanorobot individuals (20 mg ml^{-1}, 1.5 ml). Postoperative histological specimens subject to H&E(hematoxylin and eosin)- and PB(Perls Prussian blue)-staining reveal the formation of dense thrombus in the aneurysm treated under magnetic actuation, whereas no obvious filling can be found in the control group (**Figure 5c**). Following-up evaluation of the H&E- and PB-stained histological specimens after two weeks confirms the stability of the formed thrombus (**Figure 5d**). Furthermore, immunostaining demonstrates an abundance of alpha-smooth muscle actin and myofibroblast (αSMA), and macrophages (CD68) within the occluded aneurysm sac, together with abundant platelet aggregation and emerging endothelial cell lining (CD31) near the aneurysm neck (**Figure 5e**).

To exclude possible interference from other substances (than the Th encapsulated in FTP nanorobots) which could have induced the observed thrombi in the treated aneurysm, we also ligated the blood vessel to create a blind end for imitating a special aneurysm environment. Then Fe_3O_4, FP and FTP were injected into the rabbit carotid artery through a proximal indwelling needle, followed by AMF treatment to induce magnetic hyperthermia (**Figure S29**). Subsequent H&E- and PB-staining showed that only the FTP group successfully induced intra-arterial coagulation (**Figure S30**), therefore confirming the causal relationship between Th release and thrombus formation.

2.4. Safety Assessment of the FTP Nanorobots

Like other nanomedicines whose biosafety should be carefully evaluated, it is important to consider potential hazards of our FTP nanorobots. Before proceeding to *in vivo* tests, we first assessed the cytotoxicity of the FTP nanorobots (alongside Fe_3O_4, FP for comparison) *in vitro* with human umbilical vein endothelial cells (HUVECs) using a cell counting kit-8 (CCK-8) assay. No significant toxicity was observed in the HUVECs, even after 24 h incubation under high FTP concentration (200 μg ml^{-1}) (**Figures S31a-c**). In addition, a calcein AM/PI double staining assay was conducted to verify the biocompatibility of the FTP nanorobots (**Figure S31d**). Only a small amount of cell death could be detected at exceedingly high FTP concentration (400 μg ml^{-1}, 24 h incubation). The cytoskeletal organization of the HUVECs (F-actin stained) was also maintained (**Figure 6a**), consistent with the CCK-8 results. To evaluate *in vivo* safety of the aneurysm therapy, vascular endothelial tissues of the aneurysm sac subject to the embolization operation were collected for DAPI, F-actin staining and SEM imaging, where no evident disruption of the endothelial cell junctions could be identified (**Figures 6b and c**), despite the temperature rising to nearly 50 °C during the AMF-induced magnetic

hyperthermia (**Figure 4b**). Additionally, no obvious infarction or inflammatory reactions were found in tissues of the brain of the FTP-treated rabbit (**Figure 6d, Figure S32**) or the main organs of rabbits subject to FTP injection (**Figures S33 and 34**). Concomitantly, blood samples of the rabbits injected with FTP also went through biochemistry examination and hematology assays. No significant difference in the serum indexes between the PBS- and FTP-injected rabbits was noted (**Figure S35**). Taken together, these data suggest the biosafety of our nanorobots for *in vivo* applications.

3. Discussion

Metal stent-induced rejection and long-term use of oral antiplatelet agents remain major challenges in endovascular treatment of IAs, and it is highly desirable to develop more effective IA therapies with less or no reliance on metal stents. Biodegradable polymer stents have been attempted in treating coronary artery diseases and showed good application prospects[51, 52], but unsatisfactory mechanical properties impose a main limitation for clinical translation at this stage[53]. Alternatively, bioresorbable stents can fully degrade over time in the human body environment; however, undesirable restrictions such as need for recoil[54] and long degradation time[55] still hinder their clinical applications[56]. Furthermore, the use of stents themselves is tremendously limited when antiplatelet is contraindicated. Given these circumstances, the development of stent-free aneurysm treatment strategies would be of transformative importance. Previously, Zhang *et al.* designed a semisolid iodinated embolic agent (nanoclay-based shear-thinning hydrogel) to treat aneurysms and achieved desirable results both *in vitro* and *in vivo*[17]; nonetheless, immediate and complete occlusion of the aneurysm remains a challenge. More recently, Jin *et al.* developed a new type of self-adhesive microgels that can achieve spontaneous occlusion upon mild acid stimulus, yet precise delivery requires microcatheter shaping for direct injection of the microgels into the target aneurysm and therefore the *in vivo* embolization efficacy remains to be evaluated[18]. Liquid embolic agents have also been exploited for IA occlusion[57], which would allow the entire volume of an aneurysm of arbitrary shape or size to be filled. However, it is difficult to completely rinse the blood out of the aneurysm with the precursor substance, which may cause insufficient aneurysm embolization or even polymer shedding, potentially leading to infarction. Therefore, design optimization and preclinical development of embolic agents for rapid embolization and long-term stability are of imperative need to overcome existing drawbacks for feasible IA therapy.

A promising pathway can be provided by autonomously powered or remotely actuated micro/nanorobots, which have been widely explored in recent years for targeted delivery with

high-level specificity and efficiency aimed at enhanced therapeutic outcomes. One critical challenge then lies in sufficient accumulation of such micro/nanorobots carrying drug payload toward the aneurysm using agile power sources, which need to provide robust propulsion forces to contend with the viscous drag arising from arterial blood flow and support targeted delivery with high precision for controlled drug release in situ[58]. To date, crucial problems for treatment using micro/nanorobotic agents still persist, such as how to accurately locate the lesion in clinical setting and how to effectively retain the agents on site under high-flow-velocity and high-shear-force conditions encountered in intracranial arterial diseases.

To tackle the above challenges, we propose in this work a magnetic actuation-mediated strategy to achieve targeted delivery and controlled release of embolic drug for rapid embolization in situ without stent implantation or microcatheter shaping. The strategy highlights a hybrid type of FTP nanorobots, for which magnetic nanoparticles and thrombin are compactly encapsulated by a thermal-responsive protective coating made from phase-change material with tunable melting point (a design feature for designated thermal responses of the nanorobots for applications in different host environments). These FTP nanorobots can be assembled into robust collectives and driven to perform navigation in dynamic flow conditions through the controlled rotation and translation of our customized magnetic system, which generates a hybrid torque-force magnetic field. The experimental design for *in vivo* tests is to guide the FTP nanorobots for accumulation inside a model aneurysm constructed on the CCA of rabbits and local release of Th upon magnetic hyperthermia for implementing embolization, assisted by a balloon catheter for injecting the nanorobots while isolating the aneurysm from blood flow in the parent artery to warrant safety and efficacy of the treatment. For efficacy evaluation of the aneurysm therapy, we examine in detail three primary aspects which serve as the main criteria for success: (i) whether the activity of encapsulated Th can be maintained during delivery while ensuring minimal drug leakage into the blood circulation; (ii) whether localized accumulation of FTP nanorobots in the aneurysm can be achieved for targeted release of Th; and (iii) whether rapid and stable embolization can be realized without causing toxicity or undesired damage to normal tissues or organs.

We first evaluated the stability and integrity of the synthesized FTP nanorobots *in vitro* and *in vivo*. No blood clots or thrombi form when incubating the nanorobots with fresh arterial blood or injecting them into the rabbit artery, either under flow conditions or in still blood (from a constructed blind end of the artery). On the other hand, intended thrombosis can be triggered when hyperthermia is activated to melt the protective PCM coating and release the encapsulated Th. Next, we evaluated the ability of the FTP nanorobots to form tightly packed collectives for

controlled locomotion in biofluidic environments, starting with *in vitro* experiments using blood vessel mimicries followed by *in vivo* navigation of FTP nanorobots in the rabbit carotid artery under real-time tracking of ultrasound imaging. Benefiting from the dynamic control of our magnetic system under mitigated arterial flow conditions by clinical balloon catheter, robust nanorobotic collectives could form and navigate inward the target aneurysm. *In vivo* tracking confirmed the localized accumulation of the FTP nanorobots, therefore laying a foundation for subsequent *in vivo* embolization treatment as effective retention on lesion site is key to ensuring satisfactory therapeutic efficacy. Finally, following satisfactory delivery of the FTP nanorobots into the aneurysm, rapid embolization is mandatory for complete isolation of the aneurysm from the blood circulation to avoid rebleeding. In our operation, this was achieved by magnetic hyperthermia induced by an AFM device that has been proven a desired approach to circumvent the common problem of limited tissue penetration and is also relatively safe for biological tissues[59]. The embolization efficacy of the *in vivo* aneurysm therapy was confirmed through multiple clinical imaging procedures including DSA, 3D-DSA, greyscale ultrasound and CEUS. Two-week follow-up DSA angiography after the therapy further excluded the possibility of recanalization for the occluded aneurysm (previously reported for endovascular aneurysm treatment with polymeric magnetic microparticles[14]). Additionally, immune-stained (αSMA and CD68) samples of the treated aneurysm suggested its transformation into granulation tissues[17], indicating the stability of the formed thrombus. CD31 immunostaining[60] further revealed emerging endothelialization at the aneurysm neck, which would eventually isolate the aneurysm from the blood circulation and prevent aneurysm recanalization.

In the context of clinical translation, our applied dose of iron oxide nanoparticles (i.e., FTP) is within the FDA-recommended clinical dosage, stipulating a safe dose of 1020 mg or less for a 70 kg adult through Ferumoxytol administration[61], namely 14.6 mg kg^{-1}. In the present work, we have chosen a 30 mg FTP as the *in vivo* dose, corresponding to 10-12 mg kg^{-1} for the rabbits studied (body weight 2.5-3 kg). Before the animal experiments, the FTP nanoparticles were assessed to be stable and would not cause hemolysis even at high concentration. Furthermore, systematic biocompatibility assessments of tissues from the brain and other main organs of the treated rabbit in a 2-week follow-up after embolization therapy showed no infarction or inflammatory reactions. The post-operative biodistribution of Fe content in primary metabolic organs was also detected to decrease within 24 hours. As for the active component of FTP, thrombin, it naturally exists in the human body and the type of thrombin we used is a common medication in clinics. The released thrombin from the FTP nanorobot aggregates under focused hyperthermia should be embedded in the formed thrombus and isolated from the main blood

stream upon rapid embolization of the treated aneurysm, which is later on targeted at by macrophages as the CD68 immunostaining results indicate. Even if a small amount of the thrombin carried by the FTP is accidentally brought into the blood circulation, e.g., due to excess thrombin release in the occluded aneurysm, it will unlikely cause post-operative thrombosis in the parent artery as there are robust anti-coagulant mechanisms in the blood which can manage certain levels of freely-flowing thrombin to maintain homeostasis.

4. Conclusion

In summary, our integrated endovascular-nanorobotic platform has accomplished effective nanomedicine accumulation and rapid embolization of artery aneurysms without involving stents, which is a challenging task for conventional medical practices in treating intracranial aneurysms. Compared with existing stent-assisted embolization approach and potential drug delivery through catheters entering the aneurysm, which require high-level expertise and time-consuming preparations (e.g., microcatheter shaping) for patient-specific and aneurysm-dependent operations, our magnetic-actuation based and balloon catheter-assisted strategy provides a much safer and more efficient approach for precise and targeted nanoagent delivery to realize rapid aneurysm embolization with reduced drug leakage in the blood circulation. The approach applies to common intracranial aneurysm and parent artery sizes (2-7 mm), reduces undesired extracorporeal implantation, and largely circumvents side effects such as bleeding and artery stenosis. Despite the need for further improvements and more evaluations, the present study comprehensively describes an innovative biomedical engineering tool that serves as a proof-of-concept for treating targeted aneurysm in deep tissues and paves the way toward broadening applications of magnetic actuated agents for precision medicine in main arteries.

Notwithstanding the preliminary successes that have been achieved in treating rabbit model aneurysms, the therapeutic efficacy of our proposed embolization therapy using untethered FTP nanorobots is probably not yet competitive against that of conventional embolization approaches with tethered catheters for treating realistic IAs in patients. For example, with increasing distance between the magnetic actuation system and the target aneurysm, the magnetic field strength would decrease quickly, leading to weakened magnetic navigation and accumulation of the nanorobots[27]. Additionally, our current study still partially relies on catheterization and balloon dilation for temporarily attenuating the arterial blood flow to facilitate the navigation of nanorobot collectives inward the aneurysm, given that a low-strength magnetic field is applied at the moment. Therefore, future developments of our FTP nanorobots should focus on optimizing confounding factors such as field strength/operation

range of the magnetic actuation system, responsiveness of the nanorobots, as well as potential cellular interactions between the nanorobot collectives and the intravascular blood environment. The therapeutic efficacy could also be further amplified by improving the accumulation strategy of nanorobot collectives or enhancing the magnetic hyperthermia procedure. Theoretically, the hyperthermia setup is scalable to fit larger animals or even humans with magnetothermal coils enlarged to appropriate sizes. For instance, magnetic hyperthermia equipment has been reported for human application[62], with water-cooling coil equipped to keep the temperature within safe range to avoid potential damage to patients receiving treatment. To this end, larger-scale coils equipped with more advanced temperature control and cooling system will be essential. On the other hand, more physiologically realistic flow environments and complex aneurysm models in large animals should be evaluated for design optimization and preclinical developments to pave the way toward ultimate clinical translation.

5. Experimental Section

Synthesis of the FTP nanorobots. Following the preparation of Fe_3O_4 nanoparticles and the PCM (see Supplementary Methods of the SI), FTP was synthesized via a resolidification method. Two solutions, consisting of solution A (50 mg PCM and 65 mg l-α-lecithin dispersed in ethanol) and solution B (15 mg DSPE-PEG_{5k} in 30 ml Fe_3O_4 dispersion of 0.5 mg ml^{-1} containing 200 U mg^{-1} Th), were mixed by stirring at 50 °C and sonicated for 7 min. Then, the mixture was immediately cooled in an ice bath. The obtained FTP was filtrated, followed by further dialysis (14 kDa) to remove excess precursors.

In Vitro Magnetic Actuation and Hyperthermia. *In vitro* mimicries of blood vessels and aneurysms were fabricated using transparent resin through 3D printing. Blood-mimicking fluid was prepared by mixing 40% (v/v) glycerol in 60% (v/v) normal saline at room temperature. In the 3D vascular replicas, flows (0-100 ml min^{-1}) were generated using a pulsatile pump (CK15, Kamoer) following [16]. After accumulation of FTP nanorobots, the *in vitro* aneurysms were sealed on both ends with a hot-melt glue gun and moved to the AMF device (**Figure S11**, Shenzhen Shuanping Power Supply Technology Co.; SP-15A, 100 kHz, 30 kA m^{-1}, 15 kVA) for magnetic hyperthermia. A far-infrared thermal imager (Fotric 225, Shanghai Thermal Imaging Electromechanical Technology Co., Shanghai, China) was used to record the AMF process, which was then analyzed using AnalyzTR 4.1.7 software (Shanghai Thermal Imaging Electromechanical Technology Co., Shanghai, China) for acquisition of thermal images. Subsequently, the aneurysm models were weighed and digested with aqua regia on a heating plate, and ICP–OES analysis was performed using a Perkin Elmer NexIon 300X (Perkin Elmer,

Waltham, MA, USA) to measure the level of Fe content after preheating the equipment. All sample volumes used were 25 ml.

In Vivo Aneurysm Model and Embolization Therapy. All animal experiment protocols in this study were approved by the Animal Research Committee of Shanghai Jiaotong University Affiliated Shanghai Sixth People's Hospital (No. DWSY2020-0205). New Zealand rabbits (2.5–3 kg) were purchased from Laboratories (Songlian experimental animal farm, Shanghai, China), fed with standard rabbit chow and water ad libitum, and kept under automatically controlled temperature (23 ± 1 °C) with a 14-h/10-h light-dark cycle. After shaving the neck hair and fixing the limbs with the animal anaesthetized in the supine position, a 3-cm median incision was made on the neck to prepare for the implantation of an artificial aneurysm in the rabbit. First, the left common jugular vein was separated layer by layer, and the left external jugular vein (EJV) was ligated. Then, a 1.5 cm segment was sheared on one side of the ligated EJV for preparation of a venous sac. The whole segment was washed and stored in heparinized saline solution. Next, the right common carotid artery (CCA) was separated layer by layer. The arterial blood flow in the CCA was blocked with two hemostatic clamps (5 cm apart), and the artery was incised lengthwise (approximately 2 mm). After washing the lumen with heparinized saline flush, the prepared venous sac (serving as artificial aneurysm) was tightly sutured on the arterial origin using horizontal valgus mattress suture (6-0 suture).

To reduce mortality and improve the survival rate of the trial, the aneurysms were treated in time after they became established. A balloon microcatheter (Gateway, Boston Scientific) was used to inject the FTP nanorobots (20 mg ml^{-1}) into the parent artery while preventing FTP nanorobots from escaping during the embolization therapy. The AMF setup (coil diameter 10 cm) was positioned surrounding the rabbit's neck. According to the *in vitro* tests and given the degree of human cerebral ischemia tolerance, the application time for AMF upon the aneurysms was kept short, up to 5 min (513 kHz at 1001.1 A/m, 8 kW, and 28.2 A). To demonstrate the embolization efficacy of the FTP nanorobots and to exclude potential interferences, we also ligated one side of the CCA to construct a blind end for simulating the environment of an aneurysm sac and compared the coagulation results from applying Fe_3O_4, FP, and FTP of the same concentration (20 mg ml^{-1}) with or without activating AMF. All samples were injected into the blind end by an indwelling needle. The animals were euthanized after confirming the efficacy of embolization therapy (except those requiring follow-up examination after two weeks) and gross morphopathological analyses of the aneurysms were conducted by an independent pathologist.

Clinical Interventional Imaging in Vivo. A 16 million-pixel, high-end integrated digital

microscope (DOM-1001, RWD Life Science, Shenzhen, China) was used to record images and videos of the *in vitro* and *in vivo* experiments in real time. DSA, 3D-DSA and CEUS were performed to monitor the occlusion of the aneurysms constructed in the rabbit, both before and after the embolization therapy. For this purpose, the right groin fur of the rabbit was shaved after anaesthetization. With its limbs immobilized in the supine position, a 2-cm longitudinal incision was made in the right groin area to separate the muscle and fascia tissue layer by layer. Then, the right femoral artery was ligated distally, and a sheath was placed proximally. After inserting an intermediate catheter (5 French Envoy MPD, Johnson & Johnson Medical) through the femoral artery into the right CCA of the rabbit with a guide wire, rotational angiography was performed with an 5-s, 200-degree rotational run, acquiring 150 images, and a total of 7.5 ml contrast (iodixanol; Henrui Medicine, Lianyungang Jiangsu, China) injected at a rate of 1.5 ml s^{-1}; further 3D images with volume-rendering reconstruction were produced on a workstation with a 512 × 512 × 512 matrix (AW VolumeShare 5, GE Healthcare) to best display the aneurysm shape, location and neck. Then, the working projection was chosen to perform angiography (total volume 5 ml, rate 2 ml s^{-1}) to display the aneurysm. The total volume and injection speed of contrast were kept the same for the angiography procedures performed before and after treatment. For CEUS, the contrast agent (SonoVue, Bracco, Milan, Italy) was diluted by adding 5 ml normal saline and homogeneous by inversion. Sulfur hexafluoride microbubbles (2.5 ml) were injected via the guide catheter, followed by 5 ml normal saline. The aneurysm before and after occlusion were examined in both transverse and longitudinal sections.

Post-Operative Morphopathological and Immunofluorescence Analysis. To assess the effect of FTP nanorobot occlusion on the inner wall of the aneurysm sac, the rabbit carotid artery containing the saccular aneurysm was longitudinally incised to observe the tissues after embolization therapy through SEM. Tissues were fixed in 10% formalin for 24 h followed by postfixation in 1.0% osmium tetroxide for 1 h. The samples were then rinsed in ultrapure water and dehydrated in gradient ethanol. The specimens were then sputter-coated with 7 nm of gold/palladium and imaged using a Sigma HD SEM system (Carl Zeiss AG, Jena, Germany).

The expression of targeted proteins in the treated aneurysm, including alpha-smooth muscle actin (αSMA), CD68 and CD31, was determined by immunofluorescence staining of the post-operative tissues. Before the immunofluorescence analysis, paraffin-imbedded fixed tissues were sliced and prepared into slides. Tissue sections were placed in a repair cassette filled with EDTA antigen repair buffer (pH 9.0) for antigen repair in a microwave oven. After natural cooling, the slides were placed in PBS (pH 7.4) on a decolorization shaker and washed three times with shaking for 5 min each time. Subsequently, the slides were incubated overnight

at 4°C in a wet box with three primary antibodies respectively, including αSMA (A2547, Sigma), CD68 (ab213363, Abcam), and CD31 (#3528, CST). The slides were then washed three times in PBS and incubated with anti-rabbit or anti-mouse secondary antibody (GB2141 or GB2143, Ribiology) for 50 min. The slides were washed in PBS one last time and then counterstained with DAPI staining solution for 10 min before a laser confocal microscope (ECLIPSE TI-SR, NIKON) was used for image acquisition.

Evaluation of Cytotoxicity and Biocompatibility. The HUVECs purchased from the Chinese Academy of Sciences Cell Bank were cultured at 37 °C in a humidified atmosphere of 5% CO_2, and maintained in DMEM supplemented with 10% fetal bovine serum, 100 U ml^{-1} penicillin and 100 U ml^{-1} streptomycin. The cell line was authenticated by short tandem repeat DNA profiling and compared with a reference database. To quantify and visualize the cell viability, precultured cells were seeded in 96-well cell culture plates at a density of 0.5×10^4 cells per well or in 6-well cell culture plates at a density of 5×10^5 cells per well. After 24 h of cell attachment, designated samples (e.g., Fe_3O_4, FP, and FTP) were incubated with HUVECs for 12 or 24 h, after which the cell viability was measured using a Cell Counting Kit-8 assay (Dojindo, Kumamoto, Japan) and a LIVE/DEAD viability/cytotoxicity kit (L3224, Thermo Fisher Scientific). In addition, the HUVECs incubated with FTP nanorobots were also stained with tetramethylrhodamine (TRITC) phalloidin (F-actin, 40734ES75, Yeasen Biotechnology Co., Shanghai, China) and 4',6-diamidino-2-phenylindole (DAPI, C1006, Beyotime Institute of Biotechnology, Jiangsu, China) for observation of cytoskeletal organization using a confocal microscope (LSM710, Zeiss). Similarly, the vascular endothelial tissue of the aneurysm sac in the treated rabbit was also examined after embolization therapy with FTP nanorobots by cutting frozen aneurysm specimens into sections for staining and observation.

Cerebral magnetic resonance imaging (MRI) of the treated rabbit was performed with a 3T whole-body MRI system (MAGNETOM Prisma; Siemens Healthcare, Erlangen, Germany) using an 18-element anterior body coil and a 32-element posterior spine coil. The rabbit underwent axial T2-weighted turbo-spin echo (TSE T2WI) and diffusion-weighted imaging (DWI) at the same orientation. The imaging parameters for the sequences were as follows: T2WI, FOV = 79×79 mm^2, matrix size = 154×192, reconstructed resolution = 0.4×0.4 mm^2, slice thickness = 2 mm; DWI, FOV = 113×128 mm^2, matrix size = 114×160, reconstructed resolution = 0.8×0.8 mm^2, b = 0 and 1000 s/mm^2.

Statistical Analysis. No sample or data were omitted or modified from analysis. Data are presented as mean ± SD. The statistical analysis was performed using SPSS v.22.0. Two-tailed

Student's t tests were used for independent groups assuming normal distribution. * $p < 0.05$, ** $p < 0.01$ and *** $p < 0.001$ indicate significant difference.

Acknowledgements

J. Wang. and Q. Zhou. contributed equally to this work. The authors would like to thank Dr. Qing Li from Siemens Healthineers for her assistance in MRI data acquisition. This work was financially supported by the National Natural Science Foundation of China (grant nos. 82030050, 82001943, T2394534), the National Key Research and Development Program of China (2022YFC3400100), and the Fostering Project of Shanghai Health Municipal Commission for Excellent Young Medical Scholars (2022YQ063). We also thank the support from the SIAT-CUHK Joint Laboratory of Robotics and Intelligent Systems, and the Multi-Scale Medical Robotics Center (MRC), InnoHK, at the Hong Kong Science Park.

Conflict of Interest

The authors declare no conflict of interest.

Data Availability Statement

The data that support the main findings of this study are provided within the article or the Supporting Information (SI). Additional data are available from the corresponding author upon reasonable request.

Reference

[1] J. van Gijn, R.S. Kerr & G.J. Rinkel, Lancet **2007**, 369, 306.

[2] V.L. Feigin, B.A. Stark, C.O. Johnson *et al.*, Lancet Neurol. **2021**, 20, 795.

[3] M.J. Buscot, R.V. Chandra, J. Maingard, L. Nichols, L. Blizzard, C. Stirling, K. Smith, L. Lai, H. Asadi, J. Froelich, M.J. Reeves, N. Thani, A. Thrift & S. Gall, JAMA Netw. Open **2022**, 5, e2144039.

[4] C.J. Eskey, P.M. Meyers, T.N. Nguyen, S.A. Ansari, M. Jayaraman, C.G. McDougall, J.K. DeMarco, W.A. Gray, D.C. Hess, R.T. Higashida, D.K. Pandey, C. Peña & H.C. Schumacher, Circulation **2018**, 137, e661.

[5] E. Luther, D.J. McCarthy, M.C. Brunet, S. Sur, S.H. Chen, D. Sheinberg, D. Hasan, P. Jabbour, D.R. Yavagal, E.C. Peterson & R.M. Starke, J. Neurointerv. Surg. **2020**, 12, 682.

[6] A.J. Molyneux, J. Birks, A. Clarke, M. Sneade & R.S. Kerr, Lancet **2015**, 385, 691.

[7] A.J. Molyneux, R.S.C. Kerr, L.-M. Yu, M. Clarke, M. Sneade, J.A. Yarnold & P. Sandercock, Lancet **2005**, 366, 809.

[8] J. Feghali, A. Gami, S. Rapaport, M.T. Bender, C.M. Jackson, J.M. Caplan, C.G. McDougall, J. Huang & R.J. Tamargo, Neurosurgery **2021**, 88, 658.

[9] B.P. Walcott, C.J. Stapleton, O. Choudhri & A.B. Patel, JAMA Neurol. **2016**, 73, 1002.

[10] B.G. Thompson, R.D. Brown, Jr., S. Amin-Hanjani, J.P. Broderick, K.M. Cockroft, E.S. Connolly, Jr., G.R. Duckwiler, C.C. Harris, V.J. Howard, S.C. Johnston, P.M. Meyers, A. Molyneux, C.S. Ogilvy, A.J. Ringer & J. Torner, Stroke **2015**, 46, 2368.

[11] B. Chancellor, E. Raz, M. Shapiro, O. Tanweer, E. Nossek, H.A. Riina & P.K. Nelson, Neurosurgery **2020**, 86, S36.

[12] E. Pressman, C.A. De la Garza, F. Chin, J. Fishbein, M. Waqas, A. Siddiqui, K. Snyder, J.M. Davies, E. Levy, P. Kan, Z. Ren & M. Mokin, J. Neurointerv. Surg. **2021**, 13, 247.

[13] E.S. Connolly, Jr., A.A. Rabinstein, J.R. Carhuapoma, C.P. Derdeyn, J. Dion, R.T. Higashida, B.L. Hoh, C.J. Kirkness, A.M. Naidech, C.S. Ogilvy, A.B. Patel, B.G. Thompson & P. Vespa, Stroke **2012**, 43, 1711.

[14] J. Oechtering, P.J. Kirkpatrick, A.G. Ludolph, F.J. Hans, B. Sellhaus, A. Spiegelberg & T. Krings, Neurosurgery **2011**, 68, 1388.

[15] S. Kim, K.W. Nowicki, B.A. Gross & W.R. Wagner, Biomaterials **2021**, 277, 121109.

[16] J. Lim, G. Choi, K.I. Joo, H.J. Cha & J. Kim, Adv. Mater. **2021**, 33, e2006759.

[17] Z. Zhang, H. Albadawi, R.J. Fowl, I. Altun, M.A. Salomao, J. Jahanyar, B.W. Chong, J.L. Mayer & R. Oklu, Adv. Mater. **2021**, 34, e2108266.

[18] D. Jin, Q. Wang, K.F. Chan, N. Xia, H. Yang, Q. Wang, S.C.H. Yu & L. Zhang, Sci. Adv. **2023**, 9, eadf9278.

[19] S.R. Coughlin, Nature **2000**, 407, 258.

[20] G.R. Sambrano, E.J. Weiss, Y.W. Zheng, W. Huang & S.R. Coughlin, Nature **2001**, 413, 74.

[21] L. La Perna, J.W. Olin, D. Goines, M.B. Childs & K. Ouriel, Circulation **2000**, 102, 2391.

[22] G.W. Webber, J. Jang, S. Gustavson & J.W. Olin, Circulation **2007**, 115, 2666.

[23] B.J. Nelson, I.K. Kaliakatsos & J.J. Abbott, Annu. Rev. Biomed. Eng. **2010**, 12, 55.

[24] J. Li, B. Esteban-Fernández de Ávila, W. Gao, L. Zhang & J. Wang, Sci. Robot. **2017**, 2, 6431.

[25] C. Gao, Y. Wang, Z. Ye, Z. Lin, X. Ma & Q. He, Adv. Mater. **2021**, 33, e2000512.

[26] L. Sun, Y. Yu, Z. Chen, F. Bian, F. Ye, L. Sun & Y. Zhao, Chem. Soc. Rev. **2020**, 49, 4043.

[27] M. Sitti & D.S. Wiersma, Adv. Mater. **2020**, 32, e1906766.

[28] M. Ussia & M. Pumera, Chem. Soc. Rev. **2022**, 51, 1558.

[29] F. Soto, E. Karshalev, F. Zhang, B. Esteban Fernandez de Avila, A. Nourhani & J. Wang, Chem. Rev. **2022**, 122, 5365.

[30] C. Xin, L. Yang, J. Li, Y. Hu, D. Qian, S. Fan, K. Hu, Z. Cai, H. Wu, D. Wang, D. Wu & J. Chu, Adv. Mater. **2019**, 31, e1808226.

[31] B. Wang, K.F. Chan, K. Yuan, Q. Wang, X. Xia, L. Yang, H. Ko, Y.J. Wang, J.J.Y. Sung, P.W.Y. Chiu & L. Zhang, Sci. Robot. **2021**, 6, 2813.

[32] Y. Alapan, U. Bozuyuk, P. Erkoc, A.C. Karacakol & M. Sitti, Sci. Robot. **2020**, 5, 5726.

[33] H. Zhang, Z. Li, C. Gao, X. Fan, Y. Pang, T. Li, Z. Wu, H. Xie & Q. He, Sci. Robot. **2021**, 6, 9519.

[34] C. Xin, D. Jin, Y. Hu, L. Yang, R. Li, L. Wang, Z. Ren, D. Wang, S. Ji, K. Hu, D. Pan, H. Wu, W. Zhu, Z. Shen, Y. Wang, J. Li, L. Zhang, D. Wu & J. Chu, ACS Nano **2021**, 15, 18048.

[35] Z. Zheng, H. Wang, L. Dong, Q. Shi, J. Li, T. Sun, Q. Huang & T. Fukuda, Nat. Commun. **2021**, 12, 411.

[36] Y. Zhang, L. Zhang, L. Yang, C.I. Vong, K.F. Chan, W.K.K. Wu, T.N.Y. Kwong, N.W.S. Lo, M. Ip, S.H. Wong, J.J.Y. Sung, P.W.Y. Chiu & L. Zhang, Sci. Adv. **2019**, 5, eaau9650.

[37] T. Xu, J. Zhang, M. Salehizadeh, O. Onaizah & E. Diller, Sci. Robot. **2019**, 4, 4494.

[38] V. Magdanz, I.S.M. Khalil, J. Simmchen, G.P. Furtado, S. Mohanty, J. Gebauer, H. Xu, A. Klingner, A. Aziz, M. Medina-Sánchez, O.G. Schmidt & S. Misra, Sci. Adv. **2020**, 6, eaba5855.

[39] X. Yan, Q. Zhou, M. Vincent, Y. Deng, J. Yu, J. Xu, T. Xu, T. Tang, L. Bian, Y.J. Wang, K. Kostarelos & L. Zhang, Sci. Robot. **2017**, 2, 1155.

[40] J. Law, X. Wang, M. Luo, L. Xin, X. Du, W. Dou, T. Wang, G. Shan, Y. Wang, P. Song, X. Huang, J. Yu & Y. Sun, Sci. Adv. **2022**, 8, eabm5752.

[41] S. Jeon, A.K. Hoshiar, K. Kim, S. Lee, E. Kim, S. Lee, J.Y. Kim, B.J. Nelson, H.J. Cha, B.J. Yi & H. Choi, Soft Robot. **2019**, 6, 54.

[42] L. Wang, D. Zheng, P. Harker, A.B. Patel, C.F. Guo & X. Zhao, P. Natl. Acad. Sci. USA **2021**, 118, e2021922118.

[43] C. Zhou, Y. Yang, J. Wang, Q. Wu, Z. Gu, Y. Zhou, X. Liu, Y. Yang, H. Tang, Q. Ling, L. Wang & J. Zang, Nat. Commun. **2021**, 12, 5072.

[44] L. Wang, J. Wang, J. Hao, Z. Dong, J. Wu, G. Shen, T. Ying, L. Feng, X. Cai, Z. Liu & Y. Zheng, Adv. Mater. **2021**, 33, e2105351.

[45] S. Xuan, F. Wang, Y.-X.J. Wang, J.C. Yu & K.C.-F. Leung, J. Mater. Chem. **2010**, 20, 5086.

[46] W. Zou, L. Wang, J. Hao, L. Jiang, W. Du, T. Ying, X. Cai, H. Ran, J. Wu & Y. Zheng, Compos. Part. B. **2022**, 234, 109707.

[47] J. Wu, X. Cai, G.R. Williams, Z. Meng, W. Zou, L. Yao, B. Hu, Y. Chen & Y. Zheng, Bioact. Mater. **2022**, 10, 295.

[48] M. Skytioti, M. Elstad & S. Sovik, Anesthesiology **2019**, 131, 512.

[49] A. Nader-Sepahi, M. Casimiro, J. Sen & N.D. Kitchen, Neurosurgery **2004**, 54, 1343.

[50] E.H. Leach, R.A. Peters & R.J. Rossiter, Quarterly Journal of Experimental Physiology and Cognate Medical Sciences **1943**, 32, 67.

[51] J.F. Iglesias, O. Muller, D. Heg, M. Roffi, D.J. Kurz, I. Moarof, D. Weilenmann, C. Kaiser, M. Tapponnier, S. Stortecky, S. Losdat, E. Eeckhout, M. Valgimigli, A. Odutayo, M. Zwahlen, P. Jüni, S. Windecker & T. Pilgrim, Lancet **2019**, 394, 1243.

[52] S. Kufner, M. Joner, A. Thannheimer, P. Hoppmann, T. Ibrahim, K. Mayer, S. Cassese, K.L. Laugwitz, H. Schunkert, A. Kastrati & R.A. Byrne, Circulation **2019**, 139, 325.

[53] Y. Ueki, L. Räber, T. Otsuka, H. Rai, S. Losdat, S. Windecker, H.M. Garcia-Garcia, U. Landmesser, J. Koolen, R. Byrne, M. Haude & M. Joner, Circ. -Cardiovasc. Interv. **2020**, 13, e008657.

[54] H. Jinnouchi, S. Torii, A. Sakamoto, F.D. Kolodgie, R. Virmani & A.V. Finn, Nat. Rev. Cardiol. **2019**, 16, 286.

[55] Y. Onuma, P.W. Serruys, L.E. Perkins, T. Okamura, N. Gonzalo, H.M. García-García, E. Regar, M. Kamberi, J.C. Powers, R. Rapoza, H. van Beusekom, W. van der Giessen & R. Virmani, Circulation **2010**, 122, 2288.

[56] J. Wiebe, H.M. Nef & C.W. Hamm, J. Am. Coll. Cardiol. **2014**, 64, 2541.

[57] O. Poupart, A. Schmocker, R. Conti, C. Moser, K.M. Nuss, H. Grutzmacher, P.J. Mosimann & D.P. Pioletti, Front. Bioeng. Biotechnol. **2020**, 8, 261.

[58] L. Yang, T. Zhang, R. Tan, X. Yang, D. Guo, Y. Feng, H. Ren, Y. Tang, W. Shang & Y. Shen, Adv. Sci. **2022**, 9, e2200342.

[59] H. Gavilán, S.K. Avugadda, T. Fernández-Cabada, N. Soni, M. Cassani, B.T. Mai, R. Chantrell & T. Pellegrino, Chem. Soc. Rev. **2021**, 50, 11614.

[60] A. Woodfin, M.B. Voisin & S. Nourshargh, Arterioscler. Thromb. Vasc. Biol. **2007**, 27, 2514.

[61] Vasanawala SS, Nguyen KL, Hope MD, Bridges MD, Hope TA, Reeder SB, Bashir MR. Magn. Reason. Med. **2016**, 75, 2107.

[62] K. Maier-Hauff, F. Ulrich, D. Nestler, H. Niehoff, P. Wust, B. Thiesen, H. Orawa, V. Budach & A. Jordan, J. Neuro-oncol. **2011**, 103, 317.

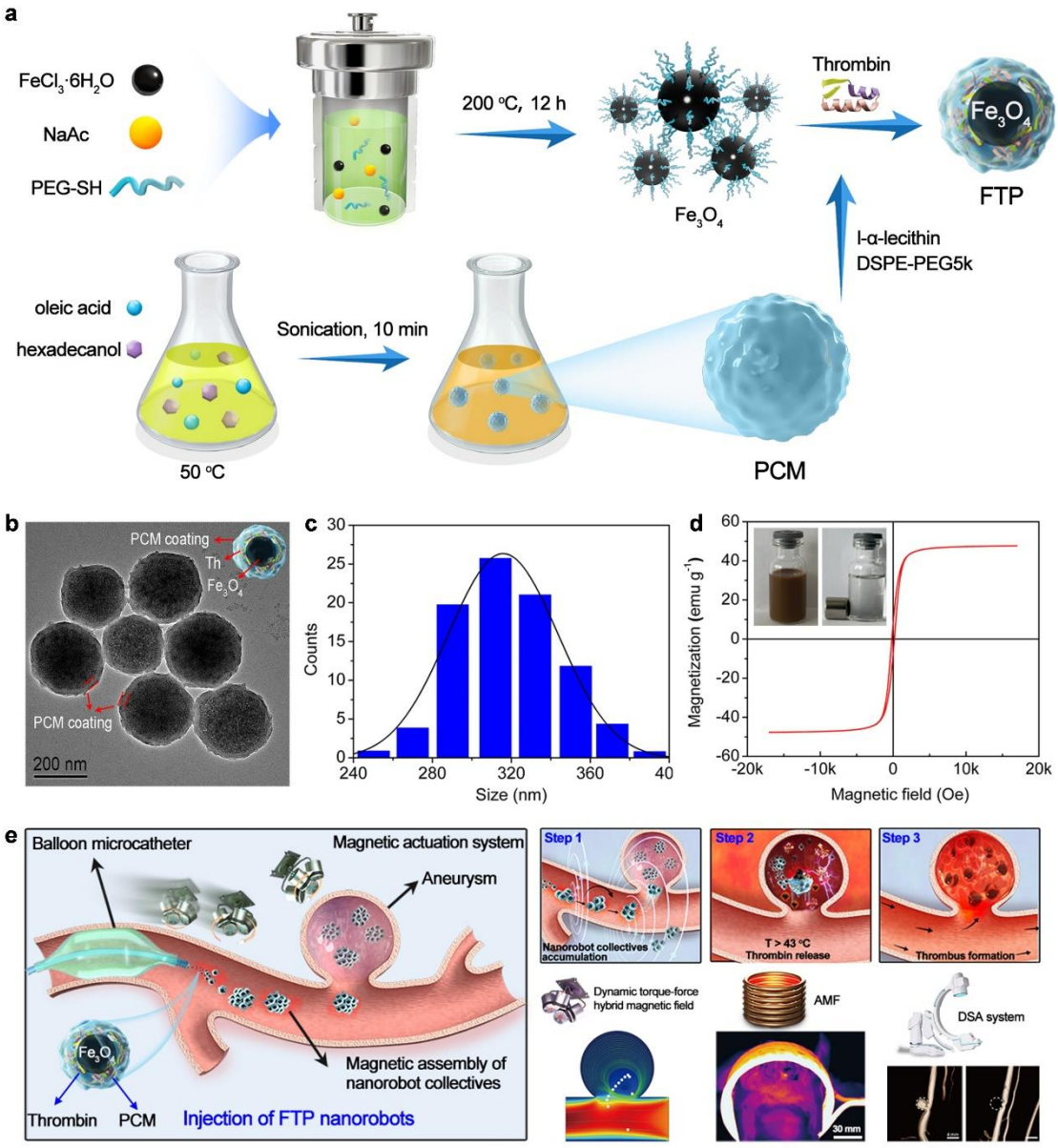

Figure 1. Fabrication of PCM-coated magnetite-thrombin FTP nanorobots and the workflow of their application for intracranial aneurysm therapy. (a) Schematic diagram of the facile fabrication process of FTP nanoparticles. First, Fe_3O_4 nanoparticles were synthesized with the solvothermal method and the PCM was prepared by mixing 1-hexadecanol and oleic acid in methanol followed by sonication. Then, the PCM was applied to co-encapsulate Fe_3O_4 nanoparticles and thrombin (Th) in compact form for yielding the final product of FTP. **(b)** Schematic (top-right inset) and TEM imaging of the FTP nanoparticles, which present spherical shapes with a mean diameter of 295 nm. The red arrows indicate the PCM coating for protecting the encapsulated thrombin (Th) from exposure to the ambient environment. **(c)** Hydrodynamic diameter distribution of the FTP nanoparticles suspended in water. The average hydrodynamic diameter of FTP was 311.2 nm measured by DLS (dynamic

light scattering). **(d)** Magnetic hysteresis curve of the FTP nanoparticles measured by VSM (vibrating sample magnetometer), which manifests superparamagnetic behavior with an *Ms* value of 47.9 emu g^{-1}. The inset shows the response of FTP nanoparticles to magnetic attraction. **(e)** Schematic illustration of the proposed workflow for thermal-responsive FTP nanorobot collectives to induce rapid embolization *in vivo* for intracranial aneurysm therapy. **Step 1**: A balloon microcatheter is employed to reduce the proximal blood flow and inject the thermal-responsive magnetic nanorobots into the parent artery of the targeted aneurysm. The nanorobot collectives form under magnetic actuation and navigate into the aneurysm sac under real-time ultrasound imaging for accumulation on site using dynamic torque-force hybrid fields through a rotary system of integrated quadrupole magnets. **Step 2**: Upon magnetic hyperthermia (MH) induced by AMF treatment, the protective PCM coating of the nanorobots responds to the thermal effect induced by the Fe_3O_4 core and burst releases the encapsulated thrombin (Th) to trigger rapid thrombus formation inside the aneurysm for embolization in situ. **Step 3**: Complete embolization of the aneurysm is evaluated and confirmed through three-dimensional DSA, contrast-enhanced ultrasound and histological analysis. PCM: phase-change material. FTP: Fe_3O_4-Th@PCM. AMF: alternating magnetic field. DSA: digital subtraction angiography. TEM: transmission electron microscopy.

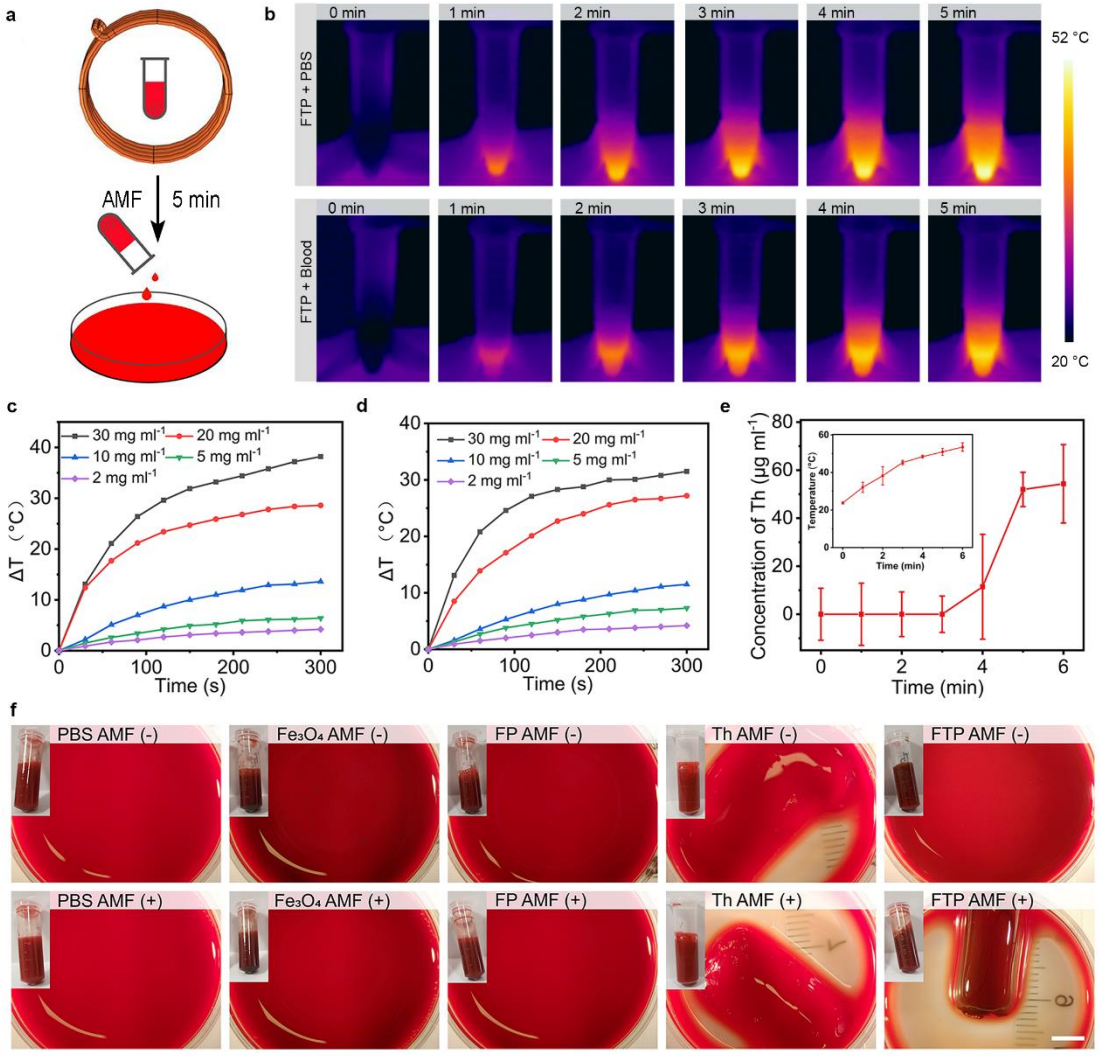

Figure 2. Characterization of the FTP nanoparticles. (a) Schematic diagram of magnetic hyperthermia (MH) of the FTP nanoparticles with an AMF coil and subsequent *in vitro* coagulation assay. For the coagulation assay, FTP samples were mixed with fresh rabbit arterial blood and heated inside the AFM coil for 5 min before pouring into a petri dish. **(b)** Time sequence of Infrared (IR) thermographic images of FTP in PBS versus FTP in fresh rabbit arterial blood subject to 5 min AFM treatment (FTP concentration: 20 mg ml^{-1}). **(c, d)** The temperature rise against MH time for different FTP concentrations in PBS (**c**) and rabbit arterial blood (**d**). **(e)** Th release curve for FTP in PBS (n =3, concentration 20 mg ml^{-1}) against MH time. The inset shows the corresponding temperature variation. **(f)** Coagulation assay for mixtures of rabbit arterial blood and different solutions, including PBS, Fe_3O_4, FP, Th (15 μg) and FTP (20 mg ml^{-1}) subject to AFM treatment. Scale bar, 5 mm. AMF (-) indicates absence of MH; AMF (+) indicates operation of MH. PCM: phase-change material. FP: Fe_3O_4@PCM. FTP: Fe_3O_4-Th@PCM. AMF: alternating magnetic field.

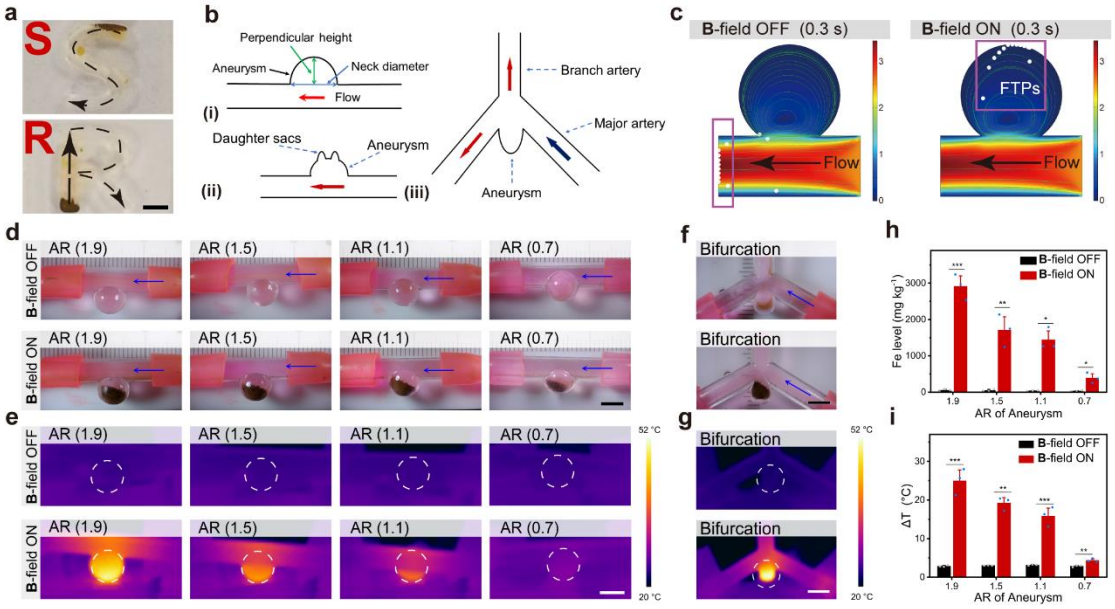

Figure 3. Controlled magnetic navigation and hyperthermia performance of the FTP nanorobot collectives *in vitro*. **(a)** Schematics of (i) the *in vitro* saccular aneurysm model with a range of aspect ratios (AR) defined as its perpendicular height divided by the neck diameter; (ii) a second *in vitro* model for lobular aneurysms with daughter sacs; and (iii) a third *in vitro* model for branching aneurysms located on a vascular bifurcation. **(b)** Magnetically guided navigation of FTP nanorobot collectives through tortuous channels of "S" shape and "R" shape (time sequence in Figure S15). **(c)** Finite-element simulation of the FTP nanoparticles in a flow of 2.5 cm s^{-1} with or without a simplified gradient magnetic field that exerts a pulling force on the particles. The rectangle or square box (purple) indicates the location of nanoparticles in the flow. **(d)** Optical images showing the accumulation of FTP nanorobot collectives (FTP concentration 20 mg ml^{-1}, 0.6 ml) in aneurysm sacs of different AR values under a flow of 2.5 cm s^{-1}, with (bottom row) or without (top row) magnetic actuation using a torque-force hybrid magnetic field. Scale bar, 5 mm. **(e)** The corresponding thermal images of the aneurysm models subject to 5 min magnetic hyperthermia (MH) following guided accumulation of FTP nanorobot collectives. Scale bar, 5 mm. **(f, g)** Optical images and thermal images of a branching aneurysm located on the apex of a bifurcation, similarly treated to the saccular aneurysms as in (d, e). **(h)** Quantification of the Fe content measured from the accumulated FTP nanorobots in (**d**). **(i)** Quantification of the temperature rise captured in (**e**). Values in (**h**) and (**i**) represent mean ± SD (n = 3; independent samples). Statistical significance and *p* values are determined by two-sided Student's t test; * $p < 0.05$, ** $p < 0.01$ and *** $p < 0.001$ indicate significant difference. B-field: "OFF" indicates no magnetic actuation; "ON" indicates magnetic actuation.

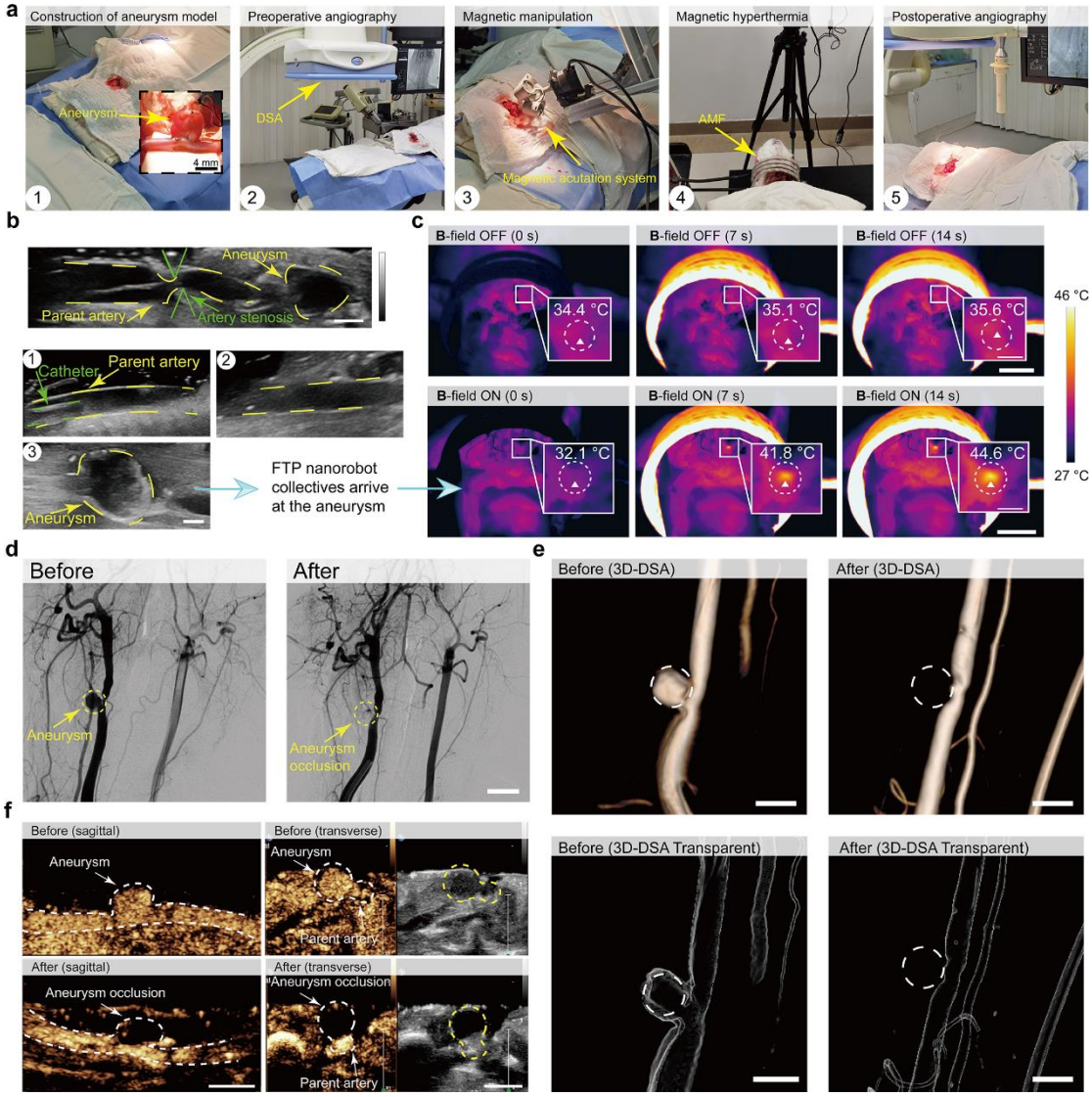

Figure 4. Occlusion treatment of model aneurysms on the rabbit carotid artery. **(a)** Procedures of the *in vivo* embolization operation, including construction of model aneurysm, preoperative DSA evaluation, injection of nanorobots under DSA, magnetic actuation and accumulation of nanorobots, aneurysm embolization with AMF-induced magnetic hyperthermia (MH), and postoperative DSA evaluation. **(b)** Real-time navigation of FTP nanorobot collectives monitored by ultrasound imaging (FTP concentration 20 mg ml^{-1}, 1.5 ml). Scale bars, 2 mm. **(c)** Thermal images of the model aneurysm during MH (total duration 15s). Scale bars: 30 mm, main frame; 5 mm, inset. **(d-f)** DSA (**d**), three-dimensional DSA (**e**), and two-dimensional greyscale ultrasound and CEUS (**f**) images of the model aneurysm before and after the embolization operation. DSA: digital subtraction angiography. CEUS: contrast-enhanced ultrasound. B-field "OFF" indicates no magnetic actuation; B-field "ON" indicates magnetic actuation. Scale bars: 10 mm (**d**); 4 mm (**e**); 5 mm (**f**).

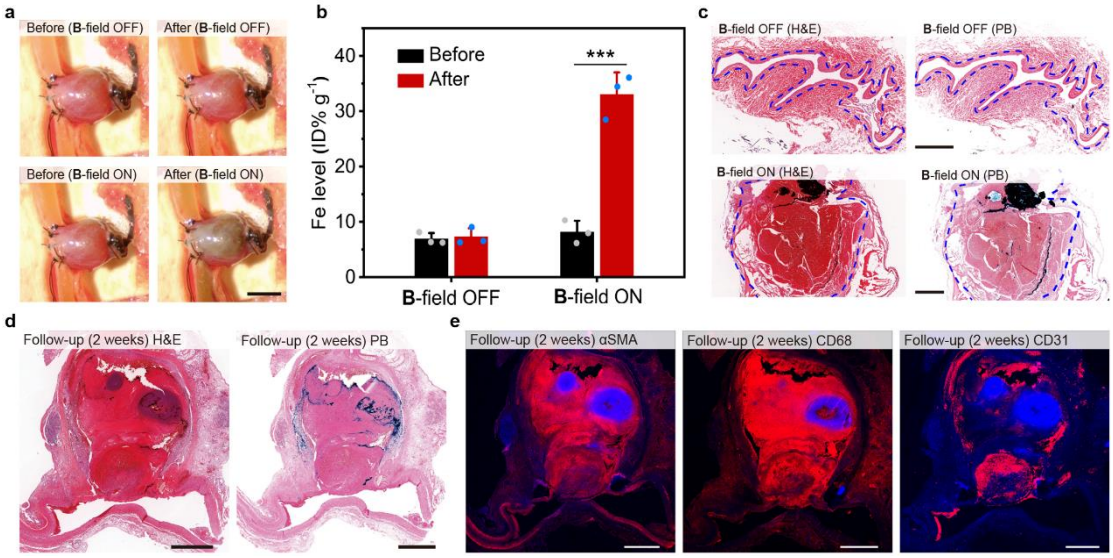

Figure 5. Magnetic actuation of FTP nanorobot collectives into the aneurysm sac and postoperative evaluation of the formed thrombus *in vivo*. **(a)** Microscope images of the rabbit carotid aneurysm experiments with or without magnetic actuation of the FTP nanorobots for accumulation (lasting for 2 min). Scale bar, 3 mm. **(b)** Quantification of FTP accumulation by determining the Fe content captured in the aneurysm sacs. **(c)** Histological images of H&E- and PB-stained aneurysm sacs shortly after FTP accumulation and magnetic hyperthermia. The dotted lines (blue) delineate the vascular wall of the aneurysm. Scale bar, 500 μm. **(d)** Histological images of H&E- and PB-stained aneurysm sacs two weeks after the embolization operation as follow-up evaluation. Scale bar, 1 mm. **(e)** Fluorescence images of αSMA (staining alpha-smooth muscle actin and myofibroblast), CD68 (staining macrophages) and CD31 (staining platelets and endothelial cells) immuno-stained aneurysm sacs obtained in the 2-week postembolization follow-up evaluation. Scale bar, 1 mm. Values in (**b**) represent mean ± SD (n = 3; independent samples). Statistical significance and *p* values were determined by two-sided Student's t test; * $p < 0.05$, ** $p < 0.01$ and *** $p < 0.001$ indicate significant difference. **B**-field "OFF" indicates no magnetic actuation; **B**-field "ON" indicates magnetic actuation. H&E: hematoxylin and eosin. PB: Perls Prussian blue.

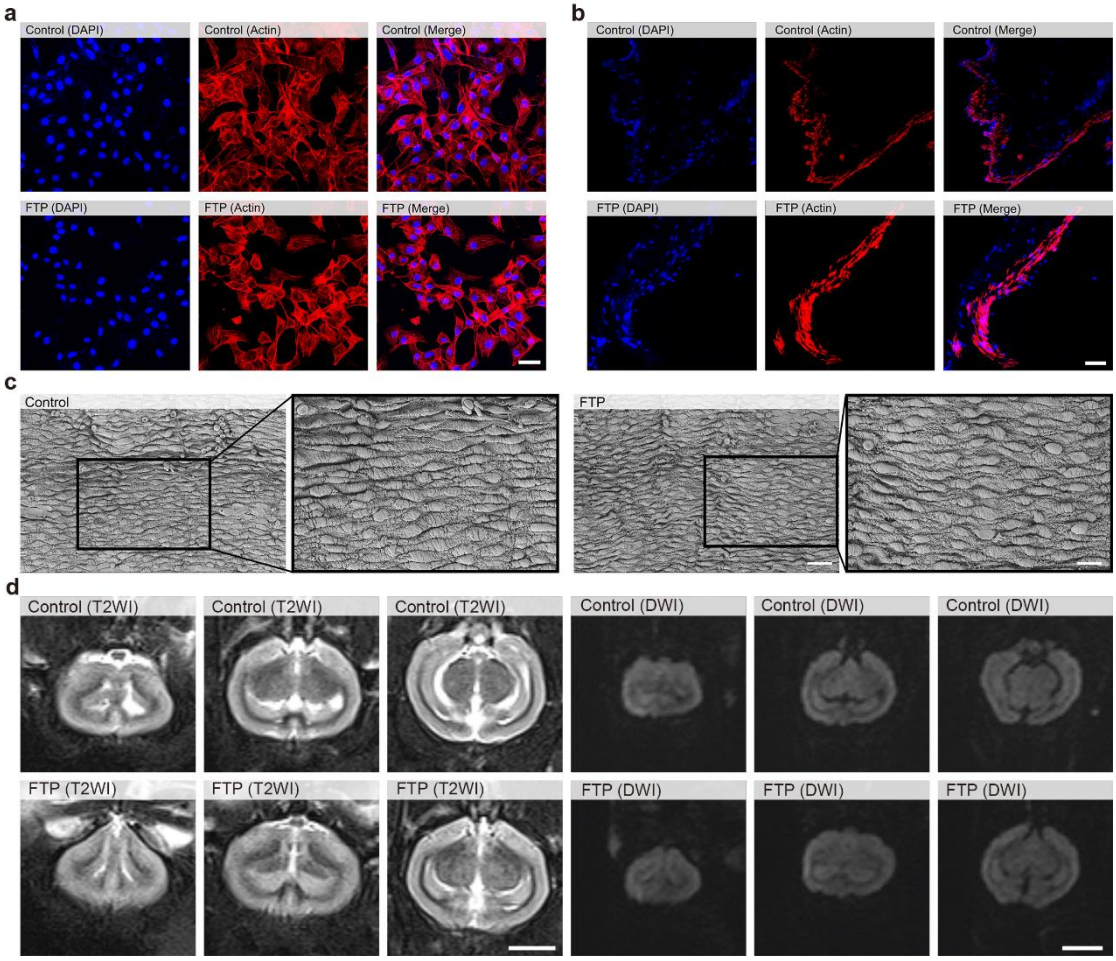

Figure 6. Biocompatibility of FTP nanorobots. (a) Fluorescence images of DAPI and F-actin stained HUVECs after 24 h incubation with FTP or without (control). Scale bar, 50 μm. **(b, c)** Fluorescence (F-actin) (**b**) and SEM (scanning electron microscopy) (**c**) images of the vascular endothelial tissues from rabbit carotid aneurysm sacs with or without (control) embolization operation using the FTP nanorobots. Scale bars: 50 μm (**b**); 20 μm, main frame of (**c**); 10 μm, inset of (**c**). **(d)** Axial view of cerebral MRI (magnetic resonance imaging) 24 h after surgery, including T2-weighted (T2WI) and diffusion-weighted (DWI) images, for FTP-treated and sham-operated (control) rabbits. Scale bar, 10 mm.

Table of Contents

A nanorobotic platform engineered to treat intracranial aneurysms (IA) through rapid and stable embolization by deploying thermal-responsive FTP nanorobots consisting of phase-change material (PCM)-encapsulated magnetite-thrombin (Fe_3O_4-Th@PCM), which synergistically integrate smart material design, secure drug packaging, agile magnetic actuation and clinical interventional imaging to circumvent exogenous implant rejection and cumbersome microcatheter shaping for quicker and safter IA therapy in clinics.

Title: Nanoarchitectonic Engineering of Thermal-Responsive Magnetic Nanorobot Collectives for Intracranial Aneurysm Therapy

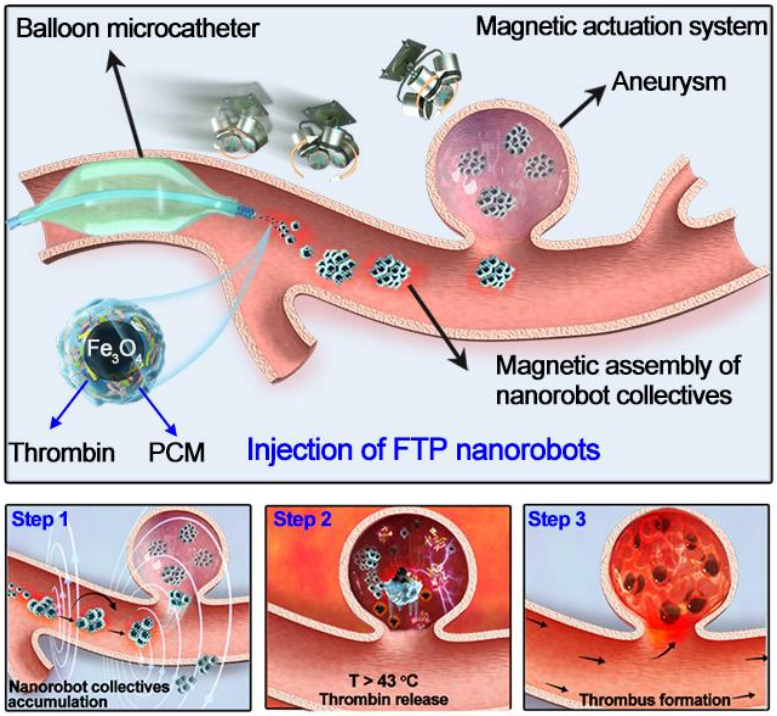

Keywords: Intracranial aneurysm, embolization therapy, magnetic nanorobots, targeted drug delivery, endovascular treatment